Supplementary Information: Density–Velocity Relation Is Scale-Dependent in Epithelial Monolayers

Hengdong Lu, Tianxiang Ma, Amin Doostmohammadi

January 8, 2026

Experimental Setup

Madin–Darby Canine Kidney (MDCK) epithelial cells were cultured in Dulbecco's Modified Eagle Medium (DMEM) supplemented with 10% fetal bovine serum and 1% penicillin–streptomycin under standard conditions. Cells were seeded onto Nunclon™ Delta-treated plastic dishes (Thermo Scientific™) and allowed to reach confluence within 24–36 h.

Time-lapse phase-contrast imaging was performed on a Nikon ECLIPSE Ti microscope equipped with a temperature- and CO_2-controlled incubation chamber (H201-K-FRAME, Okolab), maintaining cells at 37 °C and 5% CO_2. Images were acquired at 10× magnification every 10 min for a total of 8–10 h.

Local cell density was quantified using the CellSegmentationTracker Python module (https://github.com/simonguld/CellSegmentationTracker), which segments individual cells.

Velocities of individual cells were obtained from the trajectories of individual cell centers of mass extracted by the cell-tracking algorithm. For each cell i, the position of its center of mass $\mathbf{r}_i(t)$ was recorded across consecutive frames. The instantaneous velocity vector was then computed as

$$\mathbf{v}_i(t) = \frac{\mathbf{r}_i(t+\Delta t) - \mathbf{r}_i(t)}{\Delta t},$$

where Δt is the time interval between two consecutive frames (10 min in our experiments). The magnitude of $\mathbf{v}_i(t)$ gives the instantaneous speed of cell i, and ensemble averages over all cells within the field of view were used to obtain the velocity field and coarse-grained statistics described in the main text.

To measure intercellular isotropic pressure, we employed Bayesian Inversion Stress Microscopy (BISM) [9]. Substrates were embedded with fluorescent microspheres, which were imaged by epi-fluorescence during cell culture. A reference image of the relaxed substrate was acquired at the end of each experiment by adding 200 µL of 10% sodium dodecyl sulfate (SDS) or 10% Triton X-100 to detach cells. Bead images were then registered using the Image Stabilizer plugin in FIJI [5], and illumination correction was applied to reduce background noise. Displacement fields were extracted by pairwise PIV analysis in PIVlab using 32×32 pixel interrogation windows with 50% overlap. In the raw bead movies, a small number of beads are occasionally detached and diffused freely. These vectors were removed, following the established protocol [1, 9, 10]

Traction force fields were calculated via Fourier Transform Traction Cytometry (FTTC), and stress tensor fields were inferred using the BISM algorithm [9]. The isotropic intercellular pressure was computed as half the trace of the stress tensor, $(\sigma_{xx} + \sigma_{yy})/2$, with positive values denoting tension and negative values compression.

Note for Multi-phase field model

Following [8] we numerically evolve the phase field model using a finite-difference method. Phase fields are evolved on a uniform square grid with periodic boundaries. Spatial derivatives use second-order central differences, and the Laplacian uses the standard five-point stencil. Free-energy terms in Eq. (3) are integrated by Riemann sums over the grid. Time integration is explicit (forward Euler), using the update rule $\phi_i(t + \Delta t) = \phi_i(t) + \Delta t\, \partial_t \phi_i$.

Initial conditions are disks of radius R with random positions. The parameter setup is included in **Appendix Table 1** and **Table 2**. $\frac{N \cdot \pi R^2}{L^2}$ set the packing fraction. We enforce periodicity by wrap-around indexing and choose Δt to satisfy stability for the chosen grid. All dynamical data are collected after the system has evolved for a sufficiently long time to reach a non-equilibrium steady state.

The force exerted on individual cell is obtained from the tissue stress tensor σ_{tissue},

$$\mathbf{F}_i^{\text{int}} = \int d\mathbf{x}\, \phi_i \nabla \cdot \sigma_{\text{tissue}} = -\int d\mathbf{x}\, \sigma_{\text{tissue}} \cdot \nabla \phi_i, \tag{S1}$$

$$\sigma_{\text{tissue}} = \sigma_{\text{passive}} + \sigma_{\text{active}}. \tag{S2}$$

The passive stress derives from the free energy [3],

$$f_{\text{passive}} = \nabla \cdot \sigma_{\text{passive}} = \frac{\delta \mathcal{F}}{\delta \phi_i} \nabla \phi_i, \tag{S3}$$

$$\sigma_{\text{passive}} = -P\mathbb{I} - \sum_i \nabla \phi_i \frac{\partial \mathcal{F}}{\partial \nabla \phi_i}, \tag{S4}$$

$$P = -\sum_i f_i - \mu_i \phi_i, \tag{S5}$$

where f_{passive} is the passive force density, f_i is the free-energy density of ϕ_i, $\mu_i = \delta \mathcal{F}/\delta \phi_i$ denotes the chemical potential, and $\mathbb{I}$ is the identity tensor. The isotropic pressure is given by the scalar contribution of the passive stress.

For active processes, we adopt a minimal model that includes extensile shape deformations[6, 8],

$$\sigma_{\text{active}} = -\zeta \sum_i \phi_i \mathbf{S}_i, \tag{S6}$$

with activity strength $\zeta > 0$ and shape tensor

$$\mathbf{S}_i = -\int d\mathbf{x} \left[\nabla \phi_i \nabla \phi_i^T - \tfrac{1}{2} \text{Tr}(\nabla \phi_i \nabla \phi_i^T) \right]. \tag{S7}$$

This term captures the active interaction in which a cell pushes neighbors along its elongation axis and pulls them along its contraction axis.

The parameters used in this study are consistent with physiological ranges [6, 4, 2] and are listed in **Appendix Table 1**.

To test the robustness of our finding, we also included the active polar force following in phase field model, following the formulation of Ref. [7]. We set the polarization aligned with passive repulsive force, and the propulsion magnitude α is set as 6×10^{-3}. Within the simulated parameter range, the effective force generated by active stress and the polar force for individual cells lies between 2 and 10, consistent with the experimental range [6].

Static structure factor

Assuming translational and rotational symmetry, the structure factor can be equivalently calculated as

$$S(\mathbf{q}) = \langle \rho(\mathbf{q})\rho(-\mathbf{q}) \rangle = \langle |\rho(\mathbf{q})|^2 \rangle,$$

where $\rho(\mathbf{q})$ is the Fourier transform of the field $\hat{P}(\mathbf{r})$. We nondimensionalize the $S(q)$ by

$$\hat{P}(r) = \frac{P(r) - \bar{P}}{\bar{P}}$$

, where $\bar{P}$ is the average pressure of all positions. The angularly averaged spectrum was obtained as

$$S(q) = \frac{1}{2\pi} \int_0^{2\pi} S(\mathbf{q})\, d\theta,$$

where θ is the orientation of the wavevector $\mathbf{q}$. Peaks in $S(q)$ correspond to characteristic spatial length scales. All spatial lengths are in unit of cell diameter. The corresponding real-space length is related to the wavenumber by

$$r = \frac{1}{q}$$

$S(q)$ exhibits strong noise when the system size is small (**Fig.S5A**). Increasing the spatial size of simulations, a low-q peak emerges, revealing a length scale of about 7 cells.

Weaken crowding by reducing elasticity

Crowding is weakened by reducing the packing fraction (see **Fig.5C**). Furthermore, a more fluid-like regime could be obtained by reducing cell elasticity γ. In the system both elasticity and packing fraction are reduced, cells move freely and their collective dynamics become entirely driven by local active force generation, resulting in a pronounced positive correlation between density and velocity (**Fig. S6A**). Pressure segregation between high- and low-pressure regions remains pronounced, as reflected by the strong depletion in the cross-type pair-correlation function $g_{\text{cross}}(r)$ (**Fig. S6B**). In contrast, same-type correlations, $g_{\text{high–high}}(r)$ and $g_{\text{low–low}}(r)$, exhibit the hallmark of a disordered system, showing a smooth decay without pronounced peaks or oscillations.

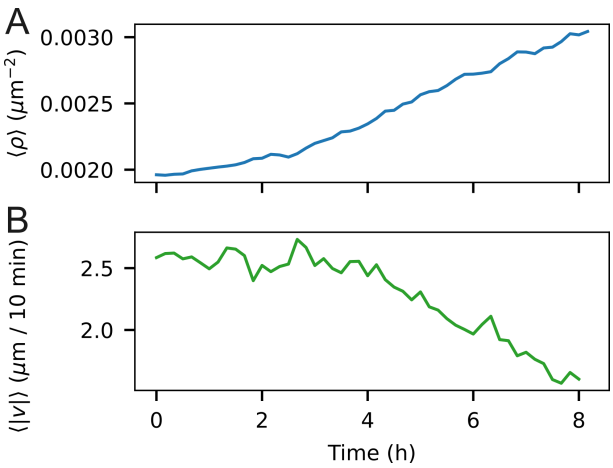

Figure S1: Temporal evolution of globally averaged density and velocity magnitude in experiments. (A) Global cell density steadily increases over the experimental time window due to proliferation. (B) The global velocity magnitude gradually decreases.

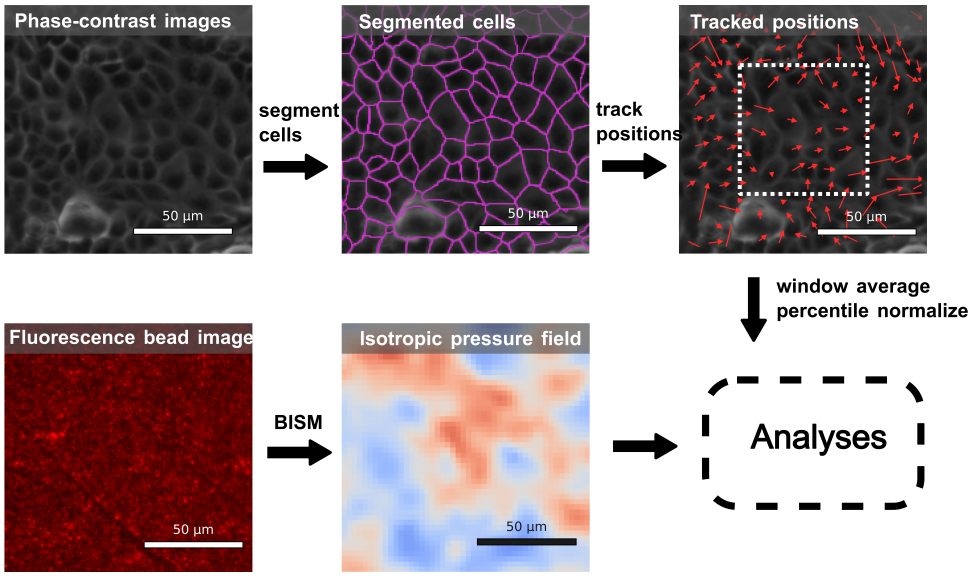

Figure S2: Complete image-processing and analysis pipeline.

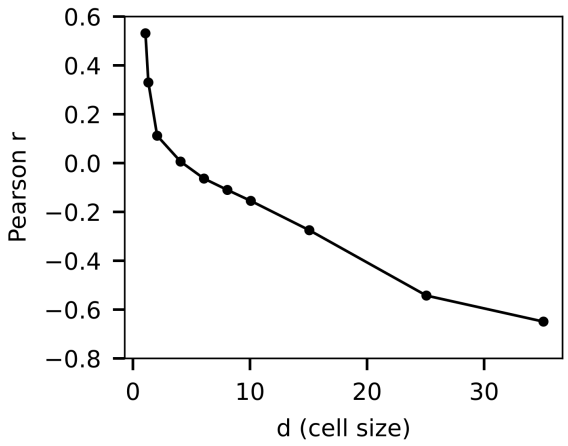

Figure S3: Pearson correlation coefficient vs window size in experiments. The Pearson correlation coefficient between normalized density and velocity shows a clear crossover from positive to negative values as the averaging window size increases. For all window sizes, the corresponding p-values are < 0.0001, confirming the statistical significance of these correlations.

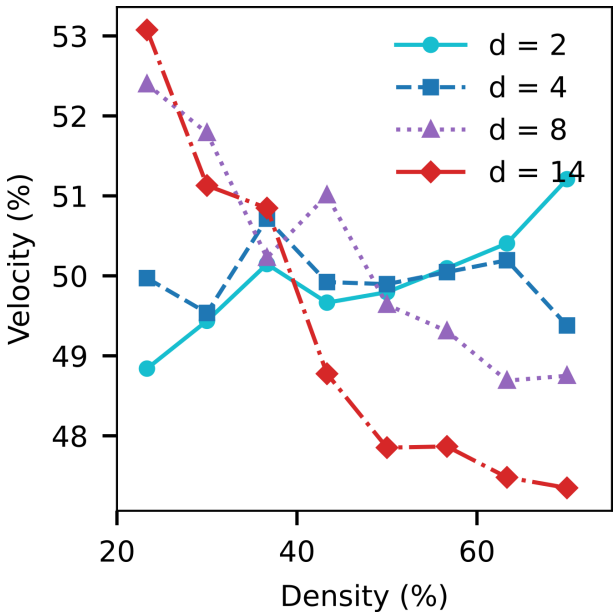

Figure S4: Scale-dependent density–velocity relation in simulations that include both active stress and polar active forces. The crossover from positive to negative correlation with increasing window size persists, demonstrating that the main result is robust to the inclusion of polar forces.

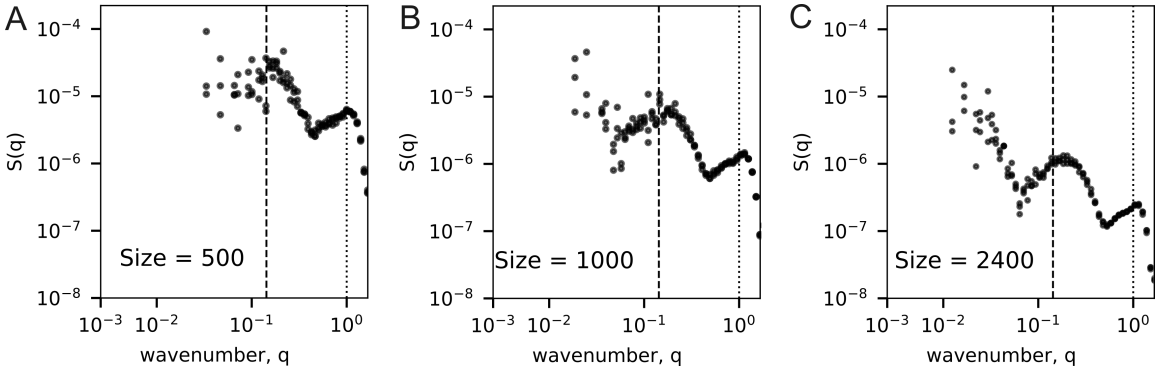

Figure S5: Structure factor of pressure field in increasingly large systems. The systems are of different sizes but identical mechanical parameters: (A) $L = 500$, (B) $L = 1000$, (C) $L = 2400$. In small systems (A), the low-wavenumber regime is dominated by noise, obscuring large-scale features. As the system size increases, a distinct low-q peak emerges, revealing a characteristic pressure length scale of ≈ 7 cells.

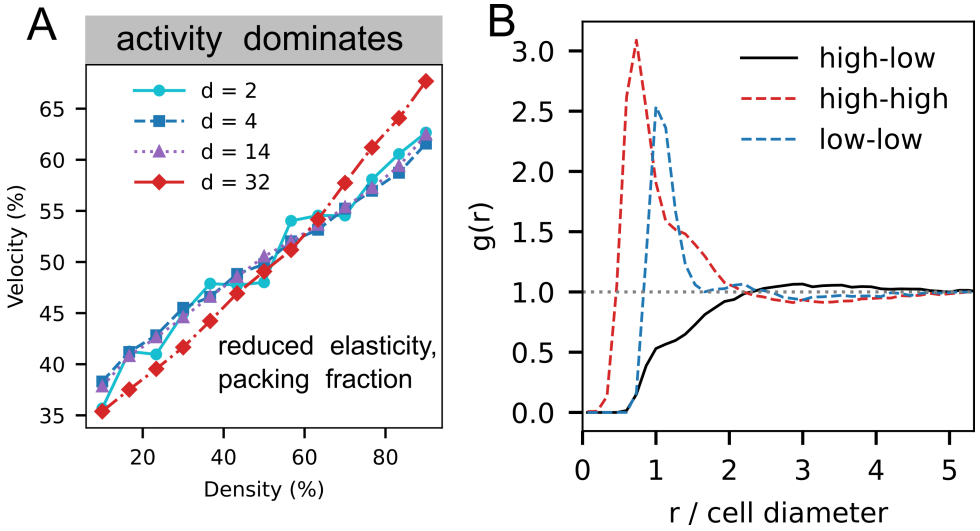

Figure S6: Crowding is weakened by reducing elasticity and packing fraction. (A) In the simulation with lower elasticity and packing fraction, density-velocity relation becomes stronger positively correlated. (B) The cross-type pair-correlation function $g_{\text{cross}}(r)$ reveals clear segregation between high-pressure and low-pressure cells, indicating spatial separation of mechanically distinct regions. In contrast, the same-type correlations, $g_{\text{high–high}}(r)$ and $g_{\text{low–low}}(r)$, exhibit the hallmark of a disordered system, showing a smooth decay without pronounced peaks or oscillations.

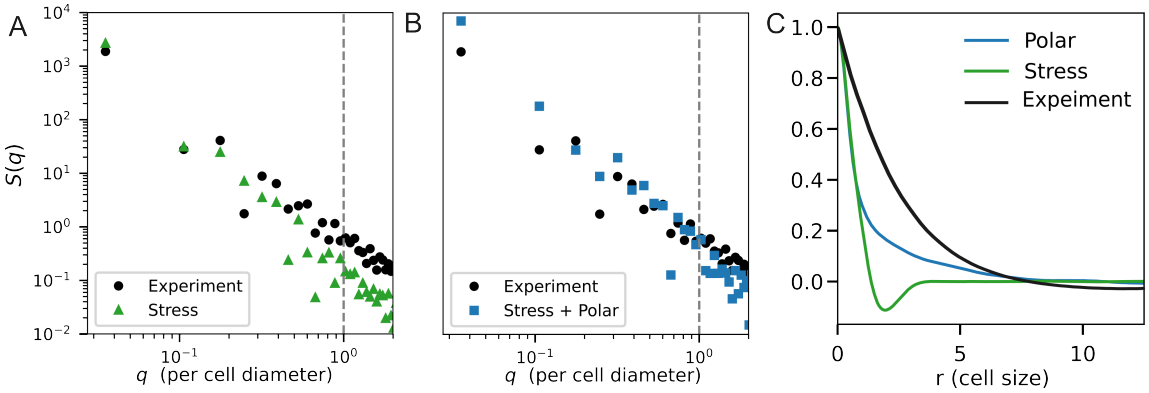

Figure S7: Effect of introducing the polar force. (A) Structure factor $S(q)$ of cell positions for the stress-only model used in the main text. (B) $S(q)$ after adding a polar force aligned with the (passive) repulsive force. Compared to experiments, the stress-only model exhibits weaker density fluctuations; introducing the polar force enhances density fluctuations and brings $S(q)$ closer to the experimental trend. (C) Velocity spatial autocorrelation function for the polar-only model, the stress-only model, and experiments, computed as the $C_v(r) = \langle \mathbf{v}(\mathbf{r}_0) \cdot \mathbf{v}(\mathbf{r}_0 + \mathbf{r}) \rangle / \langle |\mathbf{v}|^2 \rangle$, with r measured in cell-size units. The simulated systems display a shorter velocity-correlation length than experiments. Notably, the polar force yields a velocity-correlation profile closer to experiments.

Supplementary Movies

Movie. S1. Visualization of the simulated confluent cell monolayer.
Movie. S2. Raw phase-contrast images.
Movie. S3. Segmented monolayer.
Movie. S4. Computed cellular velocity.
Movie. S5. Reconstructed pressure field .
Movie. S6. Raw fluorescence bead images used for traction force microscopy.

The scale bars in **Movie. S2**, **Movie. S3**, **Movie. S4**, **Movie. S5**, **Movie. S6** are set as $200\mu m$. The temporal spacing between successive frames is 10 minutes.

References

[1] Lucas Anger, Andreas Schoenit, Fanny Wodrascka, C Rossé, RM Mège, B Ladoux, and P Marcq. Tissue stress measurements with bayesian inversion stress microscopy. *arXiv preprint arXiv:2512.00550*, 2025.

[2] Lakshmi Balasubramaniam, Siavash Monfared, Aleksandra Ardaševa, Carine Rosse, Andreas Schoenit, Tien Dang, Chrystelle Maric, Mathieu Hautefeuille, Leyla Kocgozlu, Ranjith Chilupuri, et al. Dynamic forces shape the survival fate of eliminated cells. *Nature Physics*, 21(2):269–278, 2025.

[3] Michael E. Cates and Elsen Tjhung. Theories of binary fluid mixtures: from phase-separation kinetics to active emulsions. *Journal of Fluid Mechanics*, 836:P1, 2018.

[4] Olivia Du Roure, Alexandre Saez, Axel Buguin, Robert H Austin, Philippe Chavrier, Pascal Siberzan, and Benoit Ladoux. Force mapping in epithelial cell migration. *Proceedings of the National Academy of Sciences*, 102(7):2390–2395, 2005.

[5] K. Li. The image stabilizer plugin for imagej. https://www.cs.cmu.edu/~kangli/code/Image_Stabilizer.html, 2008.

[6] Siavash Monfared, Aleksandra Ardaševa, and Amin Doostmohammadi. Multi-phase-field models of biological tissues. *arXiv preprint arXiv:2503.05053*, 2025.

[7] Romain Mueller and Amin Doostmohammadi. Phase field models of active matter. *arXiv preprint arXiv:2102.05557*, 2021.

[8] Romain Mueller, Julia M. Yeomans, and Amin Doostmohammadi. Emergence of active nematic behavior in monolayers of isotropic cells. *Phys. Rev. Lett.*, 122:048004, Feb 2019.

[9] Vincent Nier, Shreyansh Jain, Chwee Teck Lim, Shuji Ishihara, Benoit Ladoux, and Philippe Marcq. Inference of internal stress in a cell monolayer. *Biophysical journal*, 110(7):1625–1635, 2016.

[10] William Thielicke. Pivlab –towards user friendly, affordable and accurate digital particle image velocimetry in matlab. *Journal of Open Research Software*, 2(1):30, 2014.